RSC Advances

PAPER

View Article Online
View Journal | View Issue

Cite this: *RSC Adv.*, 2018, **8**, 32344

Penetrating effect of high-intensity infrared laser pulses through body tissue†

Danhong Han,[a] Jingjing Xu,[a] Zhenhai Wang,[a] Nana Yang,[a] Xunzhou Li,[b] Yingying Qian,[b] Ge Li,[b] Rujun Dai[b] and Shengyong Xu*[a]

Researchers have utilized infrared (IR) lasers as energy sources in laser therapy for curing skin diseases and skin injuries with remarkable effects. Preliminary experiments have also shown that high-intensity IR laser pulses could penetrate thick body tissues, resulting in remarkable effects for recovery from injuries in deep muscles and cartilage tissues. However, for deep-level IR laser therapy, it is unclear how much of the laser power density penetrates the body tissues at certain depths and which of the three major effects of laser irradiation, namely, laser-induced photo-chemical effect, photo-thermal effect and mechanical dragging effect, play a key role in the curing process. Thus, in this study, we developed micro-sized thin-film thermocouple (TFTC) arrays on freestanding Si_3N_4 thin-film windows as sensors for laser power density and local temperature. These devices showed excellent linear responses in output voltage to laser power density with wavelengths in the range of 325–1064 nm, and also indicated the local temperature at the laser spot. We systematically measured the penetrating effect and thermal effect through thick porcine tissues for high-intensity IR pulses with a laser system used in clinical treatment and subtracted the attenuation parameters for the porcine skin, fat and muscle tissue from the experimental data. The results offered reliable quantitative references for safe irradiation doses of high-intensity IR laser pulses in practical laser therapy.

Received 20th June 2018
Accepted 2nd September 2018

DOI: 10.1039/c8ra05285a

rsc.li/rsc-advances

1. Introduction

Laser technologies have been extensively applied in science research, industry, communication networks, military, *etc.* Lasers are also an important tool in medical applications, *e.g.*, as clean and precise cutters in surgery. In recent years, laser therapies and applications such as laser-induced hyperthermia, laser-induced interstitial thermotherapy, interstitial laser photocoagulation therapy, and laser microsurgery have been well developed.[1–3] Ultraviolet light (specifically UVB) can enable the body to produce vitamin D, which is essential for life. However, excess exposure produces harmful effects. For instance, all band UV radiation can damage collagen fibers, accelerate aging of the skin,[4] and even contribute to skin cancer by damaging DNA.[5–7] Near-infrared (NIR) light is known to be strongly absorbed by water, hemoglobin, and myoglobin. Tanaka *et al.* reported that NIR irradiation could penetrate the skin and non-thermally affect the dermis, subdermal blood plexus, superficial skeletal muscles and other tissues.[8,9] Furthermore, NIR radiation induced apoptotic changes in both the smooth muscle fibers of the subdermal blood plexus and skeletal muscle fibers of the panniculus carnosus in rats, which resulted in long-lasting vasodilation and muscle thinning. At a wavelength of 904 nm, NIR light has been shown to have antitumor activity and can increase cytomorphological changes by inducing apoptosis in neoplastic cells.[10]

When interacting with biological tissue, pulsed lasers have two main advantages compared with continuous wave lasers. The first advantage is that the high instant power in pulsed lasers allows a more efficient transfer of energy. The other advantage is that the interval between two pulses allows more efficient heat dissipation to avoid tissue thermal damage.[11,12] When interacting with biological tissues, femtosecond pulsed lasers can eliminate the thermal effect due to the extremely short energy deposition time during laser-processing, which results in precise micro-processing and highly localized structural manipulation. They are applied in living cell manipulation and clinical treatment of myopia, hyperopia, and astigmatism. Nanosecond pulsed lasers participate in various nonlinear processes *via* the localization of laser photons in spatial domains. Nanosecond pulses are applied in laser drilling and laser gravel.[13] Microsecond pulsed lasers are primarily used for low-level laser therapy (LLLT). They can accelerate mitochondrial activation, biochemical reaction rate of ATP synthesis, and

[a]*Key Laboratory for the AGA & Chemistry of Nanodevices, Department of Electronics, Peking University, Beijing, 100871, P. R. China. E-mail: xusy@pku.edu.cn; Tel: +86-10-62757261*

[b]*TED Healthcare Technology Ltd, Unit 350, 3/F, Block B, Beijing Venture Plaza, A11, An Xiang Bei li Rd., Beijing, 100101, P. R. China*

† Electronic supplementary information (ESI) available. See DOI: 10.1039/c8ra05285a

tissue metabolism as well as moderate vasodilation, increase blood supply, and reduce tissue rigidity.[14]

DNA damage is one of major concerns of laser therapy. Rastogi *et al.* reported that ultraviolet radiation (UVR) (mainly UV-B: 280–315 nm) is one of the powerful agents that can alter the normal state of life by inducing a variety of mutagenic and DNA lesions, such as cyclobutane-pyrimidine dimers (CPDs), 6–4 photoproducts (6–4PPs), and Dewar valence isomers. Ultraviolet radiation causes cleavage of DNA strand by interfering with the genome integrity.[15–17]

The safety of high-intensity lasers in the clinical and healthcare fields has attracted much attention. Among the three main interactions between the laser beam and biological tissues, namely photo-thermal, photo-mechanical (or photo-acoustical), and photo-chemical interactions,[18–20] the photo-thermal interaction is crucial considering the issue of safety.[21–23] For decades, researchers made great efforts to explore various techniques for monitoring the temperature of body tissues at deep levels during laser-induced thermotherapy, and two major technologies have been developed. For invasive techniques, thermocouples (TCs)[24,25] and fiber-optic sensors[26,27] are used as local thermal sensors. For non-invasive methods, Magnetic Resonance Imaging (MRI),[28–30] computerized tomography[31,32] and ultrasound based thermometry[33–35] are applied to measure local temperatures. The development of non-invasive methods using ultrasound imaging for temperature estimation in canine organs (*e.g.*, liver, kidney, brain, skeletal muscle, spleen and fat) can be traced back to 1979.[34] Jolesz *et al.* developed the MRI guided low-level laser therapy (LLLT) technique and investigated the capability of MR images for visualizing and distinguishing damaged tissue *via* laser irradiation.[28] Regarding invasive methods, Rao *et al.* performed the first invasive *in vivo* study employing fibre Bragg grating (FBG) sensors for monitoring the hyperthermia process, and demonstrated a resolution of 0.1 °C and accuracy of 0.2 °C in the temperature range of 30–60 °C.[27] Since the 1970s, TCs have been used to sense the changes in tissue temperature by laser therapy.[36] Manns *et al.* analyzed the overestimation of temperature caused by the direct radiation absorption of TCs in water, intralipid, and porcine tissue at different distances from the optical fiber applicator.[37] The same research group adopted the abovementioned correction for temperature monitoring during LLLT treatment for breast cancer.[38–40] Recently, van Nimwegen *et al.* performed temperature monitoring with TCs during Nd:YAG laser treatment on a canine prostate.[25] The rapid response of TCs enabled real-time monitoring of local temperatures with a delay of less than 1 ms.[41,42] Among these techniques, non-invasive thermometry commonly has unavoidable measurement errors caused by patient motion during *in vivo* applications, and its spatial resolution is limited by the size of pixels, the signal-to-noise ratio, as well as the type of tissue under investigation. Fibre-optic sensors have small size and high spatial resolution, but require complicated analysis tools and their sensitivity is affected by patient respiration. The metallic probe of commercially available TCs highly absorbs laser radiation, which may cause an artificial increase in local temperature.

The development of local temperature measurement techniques has lagged behind the development of laser therapy. For instance, in recent years, IR lasers with varied wavelengths have been found to be very effective in improving wound healing, reducing pain, anti-inflammatory, antiedematous, and particularly in deep tissue restoration and regeneration.[22,43–45] The LLLT technique applies low-power monochromatic and coherent light to injuries and lesions to stimulate healing. This therapy successfully shows pain attenuation and induces wound healing without defects.[43–49] High-intensity IR laser pulses are used in clinical treatments with the results exceeding expectations.[26,50] For example, several professional athletes treated with high-intensity IR laser pulses showed rapid recovery from sports injuries within 1–2 weeks, rather than 1–2 months under traditional physical treatment, and one of them even obtained better performances in international short distance racing competitions than he did before the laser treatment.[51]

These new developments in laser therapies led to interesting open questions. To date, it is not clear how deep the high-intensity IR laser beams or pulses penetrate human tissues and what is the local thermal effect caused by the laser at deeper levels. In high-intensity IR laser pulse therapy, the laser beam needs to penetrate 1–3 centimeters into body tissue. However, at this depth, no thermal sensors exist in the human body. In nature, biosystems sense internal and/or external temperature (T) through thermo-receptors located in or near nerve endings. The transient receptor potential (TRP) channels in the human body discriminate temperatures ranging from −10.0 °C to 60 °C.[52,53] TRPV1 is activated when T is higher than 43.0 °C,[54,55] TRPV2 is activated at $T > 52.0$ °C,[56] and TRPV3 and TRPV4 are sensitive in the range of 33.0–39.0 °C[57,58] and 27.0–34.0 °C,[59,60] respectively. Yang *et al.* pinpointed the locations of sensory spots at temperatures ranging from 40.0–50.0 °C on the backside of the hands and observed a limited number of sensors for each hand.[61] In addition to the skin, mammal mucosa and visceral organs such as the urinary bladder may also have temperature receptors.[62,63]

In this study, we developed sophisticated micro-devices on freestanding Si_3N_4 thin-film windows, which functioned as both laser power density indicator and temperature sensor, and obtained quantitative experimental data for characterization of the penetrating effects of high-intensity IR lasers pulses through thick body tissues. The results may offer valuable references for the clinical applications of high power IR lasers.

2. Materials and methods

2.1 Fabrication of TFTC arrays on freestanding thin-film Si_3N_4 window

The devices of TFTC array on freestanding Si_3N_4 thin-film windows were fabricated *via* standard cleanroom techniques on 4 inch-Si [100] wafers. Photolithography processes were performed on a MJB4 mask aligner (SUSS MicroTec, GER). The Si wafers were coated with 400 nm-thick Si_3N_4 *via* plasma enhanced chemical vapor deposition (PECVD) on both sides (performed at Microsystem Institute, Chinese Academy of Sciences, CN). Pd thin films were deposited with an electron-beam evaporator (DE400, DE Tec, CN) and Cr thin films were

deposited with a magnetron sputtering system (PVD75, Kurt J. Lesker, USA) under Ar atmosphere. Before the film deposition process, the residual photoresist on a patterned substrate was removed by oxygen plasma at a power of 250 W for 30 s in a plasma generator (PDC-M, PVA TePla, GER).

Detailed procedures for the fabrication of the freestanding Si_3N_4 windows are published elsewhere.[64–66] In brief, the TFTC arrays were first fabricated on the front side of each Si_3N_4/Si [100]/Si_3N_4 substrate. Then, a unique technique of double-side alignment with a single-side mask aligner (MJB4) was performed following the procedure developed by Wang *et al.*[64] The open windows for wet etching were patterned on the backside of each substrate and etched with an inductively coupled plasma (ICP, Technology Minilock III, TRION) system. Then, the devices on the front side were protected with plastic covers and the substrate backside was etched in 30 vol% KOH at 80–85 °C in a water bath *via* a floating technique (see Fig. S4b†). Due to the high etching rate ratio for Si [100] over Si [111], concaved pyramid-like patterns were created in the backside window in 7–8 hours, and the etching process was stopped when the penetrating square windows were seen from the front side, as shown in Fig. 1. Fig. S4c and d† show the device bond on a printed circuit board (PCB) through the standard wire-bonding process. Thermopower of the Cr/Pd TFTC sensors was calibrated on a homemade calibration platform,[42] showing a stable sensitivity of 20.99 ± 0.1 μV K^{-1}. At room temperature, the accuracy of the TFTC sensors was measured to be ±20 mK.[67]

2.2 Setup of measurement system

The practical laser treatment system tested in this study, which comprised a high-intensity Nd:YAG pulsed laser source (HIRO-3.0, ASALaser, Italy), is shown in Fig. S2a (ESI†). A photograph of the measurement system used in our cleanroom is presented in Fig. S2b,† and the measurement setup is schematically illustrated in Fig. 4. A 1064 nm near IR laser for practical clinical treatment was used as the beam source, which had a peak power of 3000 W and average power of 10.5 W. With a pulse duration of 0.06–0.1 ms and output frequency of 10–30 Hz, each laser pulse had a maximum energy of 350 mJ and a circular beam spot 5 mm in diameter. The pulse waveform is shown in the inset. Each tissue or agarose sample under investigation was put on the backside of our device, leaving a gap of 400 μm between the sample and the built-in TFTC sensors. The gap was the thickness of the Si_3N_4/Si/Si_3N_4 substrate in the etched window.

Measurements of the devices were performed at room temperature in air on a homemade platform, which comprised a sample stage, our micro-devices with built-in micro-TFTC array on Si_3N_4 thin film, a 10 × 10 multiplexer and a nanovoltmeter (Keithley 2182A). We conducted data acquisition with a computer, an NI interface card and the LabVIEW program.

2.3 Device calibration

For calibration of the devices, several types of laser systems were applied in our lab, namely, 325 nm He–Cd CW laser (1801C, KIMMON KOHAKR, JP), 488 nm diode CW laser (Advantage 263C, SPECTRA PHYSICS, US), 633 nm He–Ne CW laser (HORIBA Jobin Yvon, FR), and 785 nm diode CW laser (PC-500, Sacher Pilot, DE). The transverse mode of all the four types of lasers was the Gaussian TEM00 mode. The measurement setup in the lab is shown in Fig. S2b.† We first focused the laser without attenuator on the junction of our TFTC sensor, then fixed the height from the laser probe to the sample stage, and only changed the neutral optical attenuators in the optical path during experiments. Original laser powers of 15.3 mW, 15.1 mW, 34.9 mW and 79.2 mW were used for the 325 nm, 488 nm, 633 nm and 785 nm lasers, respectively. For sensitivity testing of the TFTC device on the Si_3N_4 window, 6 different attenuators (namely, D0.3, D0.6, D1, D2, D3, and D4, Thorlabs, US) were used in the laser path to adjust the irradiation intensity on the TFTC device from 100% to 60%, 30%, 10%, 1%, 0.1%, and 0.01%, respectively. With the attenuation of the laser intensity, the laser spot dimension decreased from 40 μm to 5 μm. For each measurement, the output of the TFTC sensor was recorded for 10 s, and then the laser path was blocked for 60 s. This process was repeated 5 times. Four TFTC sensors on one testing window (Fig. 1) were measured individually, and their data were averaged as the measurement results.

2.4 Preparation of agarose samples and body tissues

Samples of bulky agarose, porcine tissues and beef tissues were used in this study. Agarose samples were made from a mixture of 3 vol% agar powder (K1001, JP) in deionized water. The mixture was heated to boil, and then poured into a mold for cooling to room temperature. Samples of 15 mm × 15 mm squares with a thickness of 7.2 mm, 10 mm, 15 mm, 20 mm, 30 mm, 40 mm and 50 mm, and 60 mm were prepared. Four types of porcine tissues, namely, fat (F), skin-fat (SF) combination, muscle (M(p)), and skin-fat-muscle (SFM(p)) combination, and one type of beef muscle (M(b)) were purchased from a nearby supermarket several times. The fresh meats were usually prepared (as food) on the same day or one day before. Then, we cut the bulky meat into a shape of 20 mm × 20 mm and thickness (t) of 1–30 mm. The porcine skin had only one thickness of 1–1.5 mm.

Before testing the body tissues with the 1064 nm high-intensity Nd:YAG pulsed IR laser, the laser system was turned on, stabilized and calibrated for background data for 1 minute. Each measurement lasted 0.5–2.0 minutes. Then, the process was paused for 5 minutes to let the sample temperature go back to its original value. After the pause, we repeated the measurement procedure or started a set of new experiments with new parameters.

3. Results and discussion

3.1 Performance of TFTC arrays on Si_3N_4 thin-film windows

Fig. 1 presents a group of photos of one typical micro-TFTC array on freestanding 400 nm-thick Si_3N_4 thin-film windows. The hot-ends (sensing junctions) of the Cr/Pd TFTC arrays are located on nine 280 μm × 280 μm square freestanding Si_3N_4 windows at the center of each testing device, as shown in the

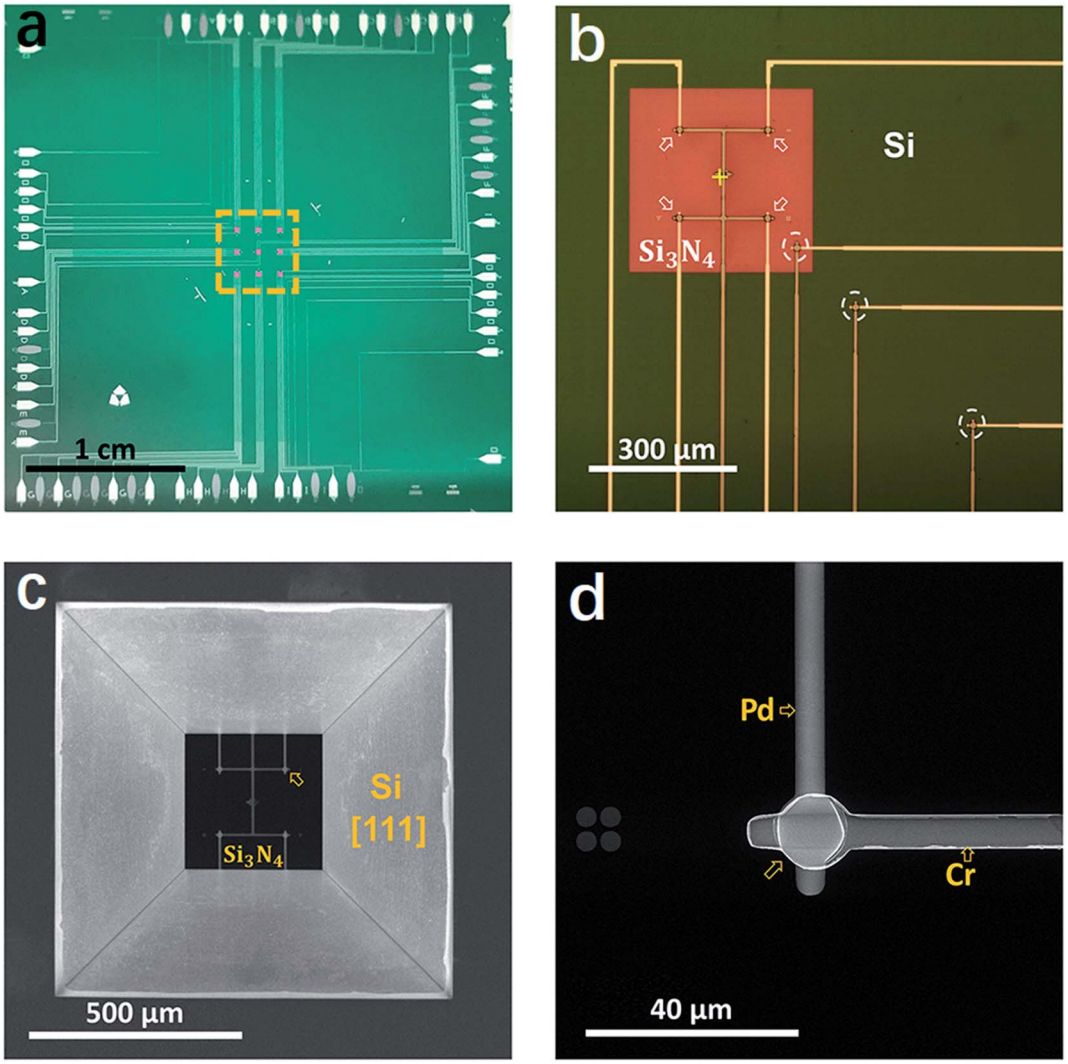

Fig. 1 Images of one typical micro-TFTC array on Si_3N_4 window. (a) The entire structure, which has nine freestanding Si_3N_4 windows at the center of the device. (b) Optical micrograph of one Si_3N_4 window, in which there are four sensing junctions of Pd/Cr TFTCs. (c) Scanning electron microscopy image showing a backside view of one Si_3N_4 window with four built-in TFTCs, in which four Si [111] surfaces are clearly seen in a pyramid-like structure. (d) A sensing junction of the TFTC in the SEM image.

orange dashed square in Fig. 1a, and the cold-ends of the TFTCs are located at the device edges, 1.5–2.0 cm away from the testing zone. On each Si_3N_4 window, there are four sensing junctions of Pd/Cr TFTCs, as marked by the arrows in Fig. 1b, where the Cr beam appears darker than the Pd beam. Two groups of reference thermocouples with an increased proportion were set up in the upper left and lower right corners of the device. Their role was to monitor the spread of the laser temperature on the device and to calibrate the temperature of the cold-ends. There are three reference thermocouples, which are highlighted by the white dotted circles in Fig. 1b. Fig. 1c shows the scanning electron microscopy image, displaying the backside view of one Si_3N_4 window with four built-in TFTCs. Four Si [111] surfaces are clearly seen in a pyramid-like structure, which are created *via* a floating KOH etching process on the Si_3N_4/Si(100)/Si_3N_4 wafer.[64,65] For this device, the alignment error between the front-side TFTC pattern and the backside Si_3N_4 window was measured to be only 5 μm. Fig. 1d presents the SEM image of the sensing junction of a TFTC from the backside, where the Cr beam overlaps on top of the Pd beam, which has a diameter of 5 μm.

Compared with the same TFTC sensors made on solid Si wafers, the sensors fabricated on freestanding Si_3N_4 windows had improved sensitivity to laser irradiation. Fig. 2 presents a typical group of comparative experimental results. Fig. 2a and c are the optical photos of two types of TFTC arrays fabricated on freestanding Si_3N_4 windows, which appear brown in the surrounding dark green Si substrate. In the device shown in Fig. 2a, the four TFTC sensing junctions (marked by arrows) share one common Cr beam (highlighted in the figure). In contrast, for the four sensing junctions in Fig. 2c, each has an independent Cr beam. According to our previous results, the structure in Fig. 2a saves nearly half of the leads and cold-end connections and simultaneously maintains measurement

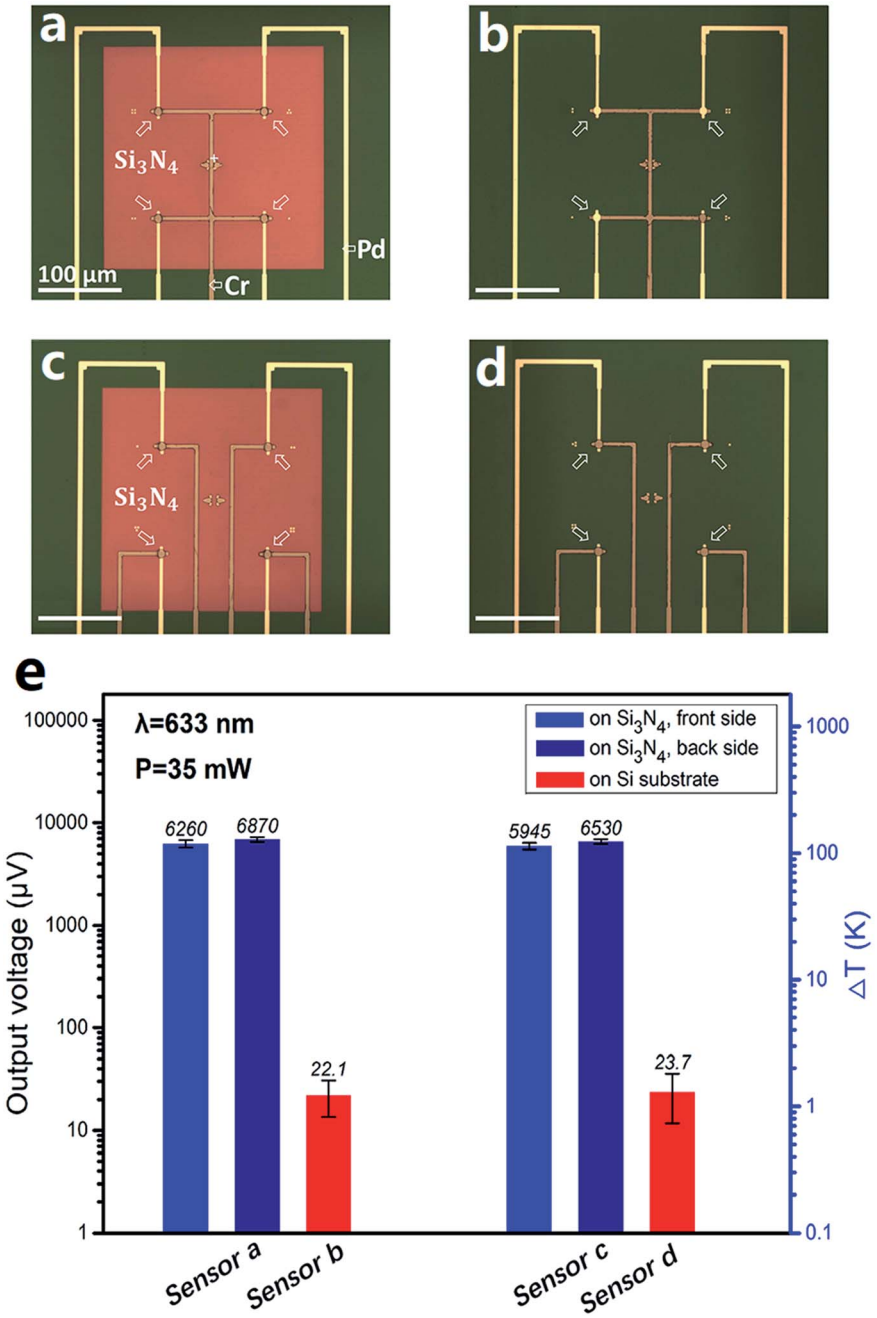

Fig. 2 Test sensitivity of the micro-TFTC array on Si_3N_4 window. (a)–(d) Two different TFTC structures are shown in the Si_3N_4 window and Si substrate. (e) Voltage outputs of the structures shown in (a)–(d) under the same irradiation of a laser spot with a wavelength of about 633 nm and laser power of 35 mW. The mazarine bar represents a laser beam shined onto the TFTC sensors from the backside of the Si_3N_4 window, the blue bar represents the front side testing mode, and the red bar represents a laser beam shined onto the TFTC sensors on Si substrate.

accuracy of the device with an error within 5%.[68] For comparison, devices with exactly the same shape, parameters and same materials were fabricated on a solid Si substrate, as shown in Fig. 2b and d. The voltage outputs of these TFTC sensors under the same irradiation of a laser spot (wavelength 633 nm, laser power 35 mW) are plotted in Fig. 2e. The sensors sharing a common Cr beam (Fig. 2a), for instance, the sensor on the freestanding Si_3N_4 windows, gave an average output of 6260 ± 500 μV, while that on solid Si gave an average output of 22.1 ± 15 μV, which is 290 times lower. Similarly, the sensors shown in Fig. 2c gave an average readout signal of 5940 ± 440 μV, but the average output for the sensors shown in Fig. 2d was only 23.7 ± 12 μV, which is 250 times lower.

We may note that the relative measurement error for the TFTC on the solid Si wafers (around 70%) is much larger than that on the Si_3N_4 window (around 8%). The thermopower of our Cr/Pd TFTC sensors was 21.0 ± 0.1 μV K^{-1}.[67] An output of 5900–6300 μV corresponds to an increment of 280–300 K in the local

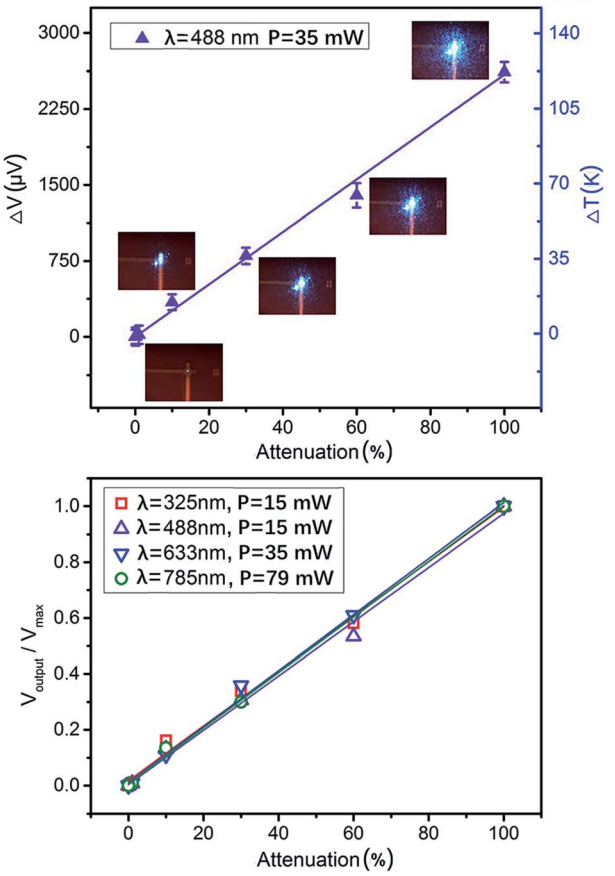

Fig. 3 Lasers of four different wavelengths, 325 nm, 488 nm, 633 nm and 785 nm, were measured with the TFTC array on Si3N_4 window in different attenuation modes. (a) Measurement results for the 488 nm wavelength. (b) Measurement data for the four wavelengths normalized individually and plotted together.

temperature at the sensing junction region and the temperature of the cold-ends, which are supposed to be kept at room temperature. However, an output of 22–23 μV only corresponds to an increment of 1 K. In addition, the local heat under laser irradiation diffuses rapidly in the thick solid Si substrate underneath the TFTC sensors. These factors result in large fluctuations in the outputs of the TFTC sensors made of solid Si.

We observed that when a laser beam shined onto the TFTC sensors from the backside of the Si_3N_4 window, the outputs of our device were larger than that measured when the laser shined from the front side. For instance, under the same 633 nm laser beam, the backside configuration testing mode measured 6870 ± 370 μV, which is 9.7% higher than the output of 6260 ± 500 μV for the front side testing mode. This may have resulted from the low reflection of the laser beam due to the Cr and Pd beams and more penetration of the laser passing through the Si_3N_4 thin film. The results are summarized in Fig. 2e. Therefore, in the experiments for testing the penetration effects of lasers with varied wavelengths, our devices were all placed upside down. This not only increased their sensitivity, but also prevented contamination of the sensors from wet tissue materials under testing and shortage of the device leads.

Our TFTC sensors on freestanding Si_3N_4 windows showed good linear response to the intensity of incident laser beams at different wavelengths. Four different wavelength lasers, 325 nm, 488 nm, 633 nm and 785 nm, were measured with the TFTC array on the Si_3N_4 window (Fig. 1 and 2a). Neutral optical attenuators were used in the laser path, so that the irradiation intensity on the TFTC device was adjusted from 100% to 60%, 30%, 10%, 1%, 0.1%, and 0.01%. Fig. 3a shows the plot of one set of the raw measurement results. The insets are the laser spot images at the TFTC surface taken with a CCD camera. The spot size shrinks with a decrease in intensity. The outputs of the device show good linearity with the irradiation intensity. Since the laser spot on the device changed its shape slightly and its size remarkably when the laser path was interrupted with different optical attenuators, some measurement data (*e.g.*, at 60% intensity) differed slightly from the linear fitting line. In Fig. 3b, the measurement data for four wavelengths are normalized individually and plotted. The maximum power for the wavelengths of 325 nm, 488 nm, 633 nm and 785 nm is 15.3 mW, 15.1 mW, 34.9 mW and 79.2 mW, respectively. The results for the attenuated laser power at full wavelength are presented in Table S1 (ESI†). Under this condition, the lasers from ultraviolet (UV) to infrared wavelength all result in linear response outputs for the devices under investigation.

TFTCs are thermal sensors. Under laser spots of wavelengths of 325 nm, 488 nm, 633 nm and 785 nm and incident power of 15.3 mW, 15.1 mW, 34.9 mW and 79.2 mW, average outputs of 3950 ± 200 μV, 2615 ± 130 μV, 5870 ± 280 μV, and 16 100 ± 800 μV were measured in 10 seconds, corresponding to absolute increments of local temperature 188 ± 9.4 K, 125 ± 6.2 K, 280 ± 14 K and 765 ± 35 K at the hot end (junction region) over the cold end, respectively.

Thus, we conclude that our TFTC arrays fabricated on Si_3N_4 thin-film windows are excellent sensors for laser power density in the measurement range of this study. When the laser intensity increases, nonlinearity in the device response (output) may occur. Hence, we tested the limit at which the linear response of our devices starts to fail. For instance, when the laser power of wavelength 785 nm was set to 79.2 mW, we measured a peak output of 49 300 μV under one second. This corresponds to a peak temperature of 2350 K, which is higher than the melting points of the Cr and Pd films (2130 K and 1828 K, respectively); hence, the junction region device melted and the device failed (see ESI Fig. S1†).

3.2 Penetration of laser over polymer and biological tissue

We set up a special platform for the measurement of the penetration effect of a laser beam passing through body tissues. Fig. 4 schematically presents the major elements of the platform, and an optical photograph of the system is presented in the ESI in Fig. S2.† In brief, before each measurement, the laser beam under investigation was guided to focus on one of the nine Si_3N_4 windows with built-in TFTC arrays. The testing device was placed upside down so that the Cr/Pd TFTCs and contacts were all under the Si_3N_4 window or Si substrate. Then, a piece of rectangular sample with the desired thickness was

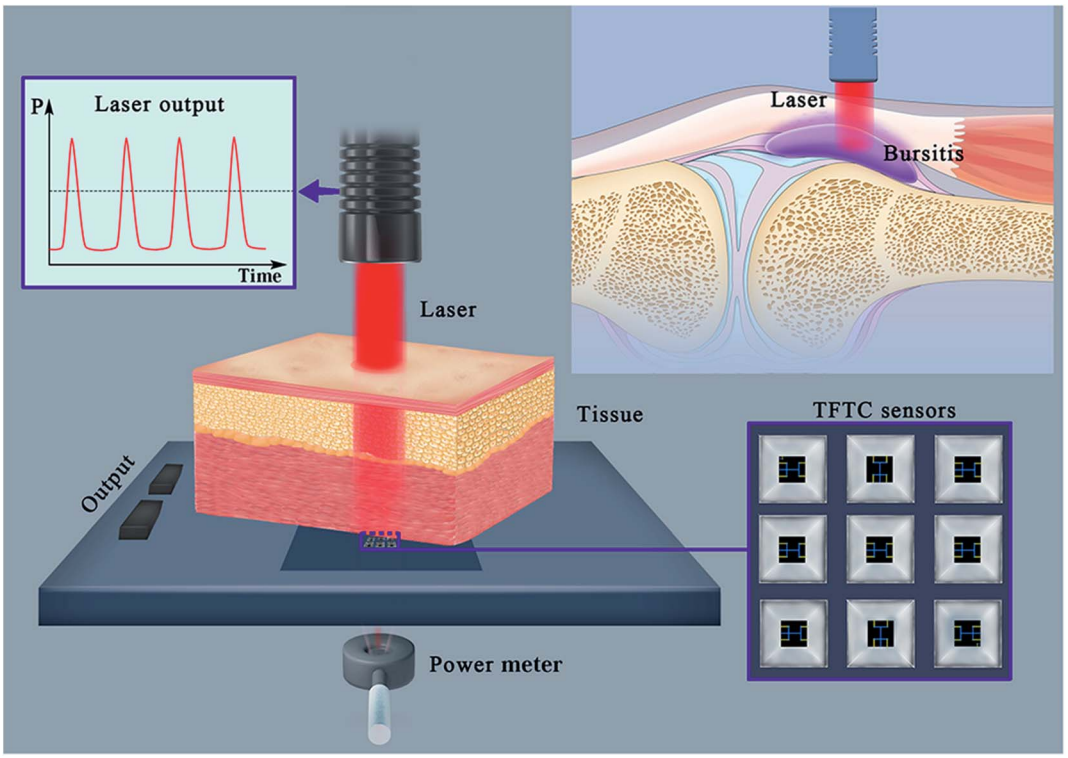

Fig. 4 Schematic of the platform for the measurement of the penetration effect of a laser beam passing through body tissue showing the major elements of the platform. A laser beam focuses on one of the nine Si_3N_4 windows with built-in TFTC arrays and then, a piece of rectangular sample with the desired thickness is loaded directly on the substrate, covering the TFTC array. This allows the laser beam to penetrate the sample before being measured with the TFTC sensors. The inset is a demonstration of the medical laser in the treatment of soft tissue damage.

loaded directly onto the substrate, covering the TFTC arrays; thus, the laser beam needed to penetrate it before measurement with the TFTC sensors.

We calibrated the measurement platform with bulky agarose (solidified from 3% agar gel) of varying thickness from 7 mm to 60 mm, and the 1064 nm IR laser beam from a high-intensity Nd:YAG pulse laser system was applied. Fig. 5a shows the plots of the raw measurement curve of the TFTC outputs *versus* time at varied incident mean power density of 3.6 W cm^{-2}, 7.2 W cm^{-2}, 10.2 W cm^{-2}, 21.4 W cm^{-2}, 35.6 W cm^{-2} and 53.4 W cm^{-2}, namely, P_1, P_2, to P_6, for samples with thickness of 7.2 mm, 15 mm, 20 mm, 30 mm, 40 mm and 50 mm, respectively. Fig. 5b shows the plot of the outputs of TFTC for a 7.2 mm-thick agarose sample under six different laser intensities, showing a linear response of the TFTC sensor to the incident laser power density. In Fig. 5c, all six sets of maximum outputs are plotted for the curves shown in Fig. 5a, revealing the sample thickness at different laser intensities.

Based on tissue characteristics, researchers have used different models to analyze laser propagation under multiple scattering conditions. The scalar stationary radiation transfer theory (RTT) is valid for an ensemble of scatterers located far from each another and has been successfully used to work out some practical aspects of tissue optics.[69–71] The two-flux Kubelka–Munk (KM) model can be used to separate the light beam attenuation due to absorption from the loss due to scattering in one dimension (1D).[71–73] The IAD method provides a tool for the rapid and accurate solution of inverse scattering problems.[71,74,75] However, the IMC method should be used to obtain reliable estimates.[71,76,77]

By ignoring the broadening effect of the laser beam, we can use the Bouguer–Beer–Lambert law directly to determine the laser transmission coefficient and effective laser penetration depth for a sample as follows:[71,78]

$$I(d) = (1 - R_F) I_0 \, e^{-\mu_t d} \quad (1)$$

where $I(d)$ is the intensity of the transmitted laser (W cm^{-2}) and R_F is the coefficient of Fresnel reflection at the normal beam incidence ($R_F = \frac{(m-1)^2}{(m+1)^2}$, where m is the relative mean refractive index of tissue and surrounding medium of the incident half-space. For an NIR laser and typical biological scatterers $m = 1.05 - 1.10$) I_0 is the incident light intensity (W cm^{-2}). $\mu_t = \mu_\alpha + \mu_s$ is the interaction or total attenuation coefficient including the laser absorption coefficient and laser scattering coefficient. The effective attenuation length $L_t = \frac{1}{\mu_t}$ is the distance where the intensity reduces to 1/e of its maximum value.

As shown in Fig. 5d, when the output voltage data, V, is plotted in logarithmic coordinates, the thickness data, t, remains linear. The results shown in Fig. 5b–d again prove that our TFTC arrays on freestanding Si_3N_4 thin-film window are excellent sensors for laser power density at a wavelength of 1064 nm, and when this IR laser beam penetrates agarose bulk,

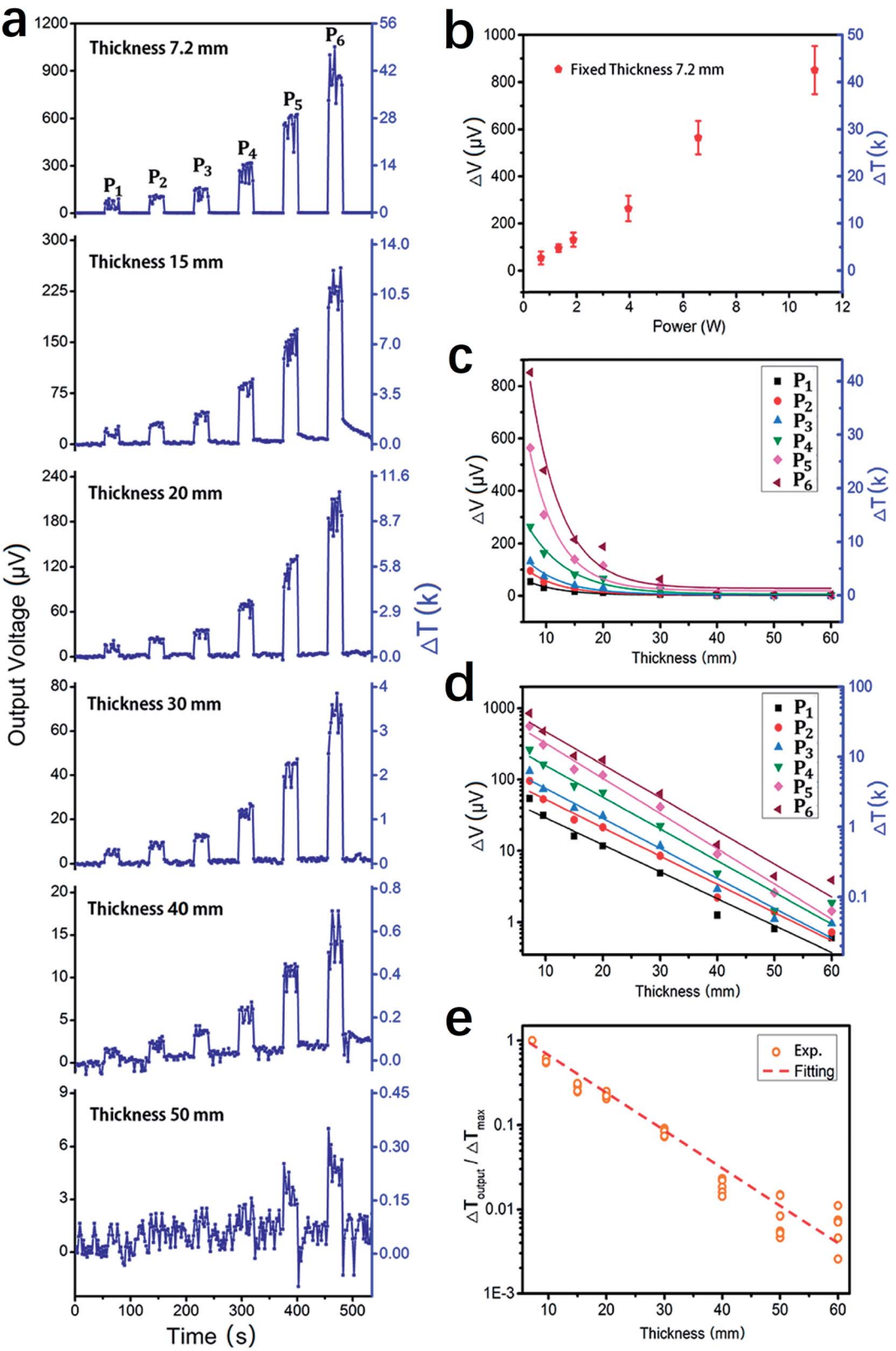

Fig. 5 3 vol% bulky agarose with varying thickness ranging from 7 mm to 60 mm used to calibrate the measurement platform. (a) Raw measurement curves of the TFTC outputs *versus* time at varying incident average power densities of 3.6, 7.2, 10.2, 21.4, 35.6 and 53.4 W cm^{-2}, namely, P_1, P_2, to P_6, for samples with a thickness of 7.2, mm, 15 mm, 20 mm, 30 mm, 40 mm and 50 mm, respectively. (b) Outputs of TFTC for a 7.2 mm thick agarose sample under six different laser intensities. (c) Maximum outputs with an increase in sample thickness at different laser intensities. (d) Results from (c) in logarithmic coordinates. (e) Result from the fitting of the normalized experimental data in (d).

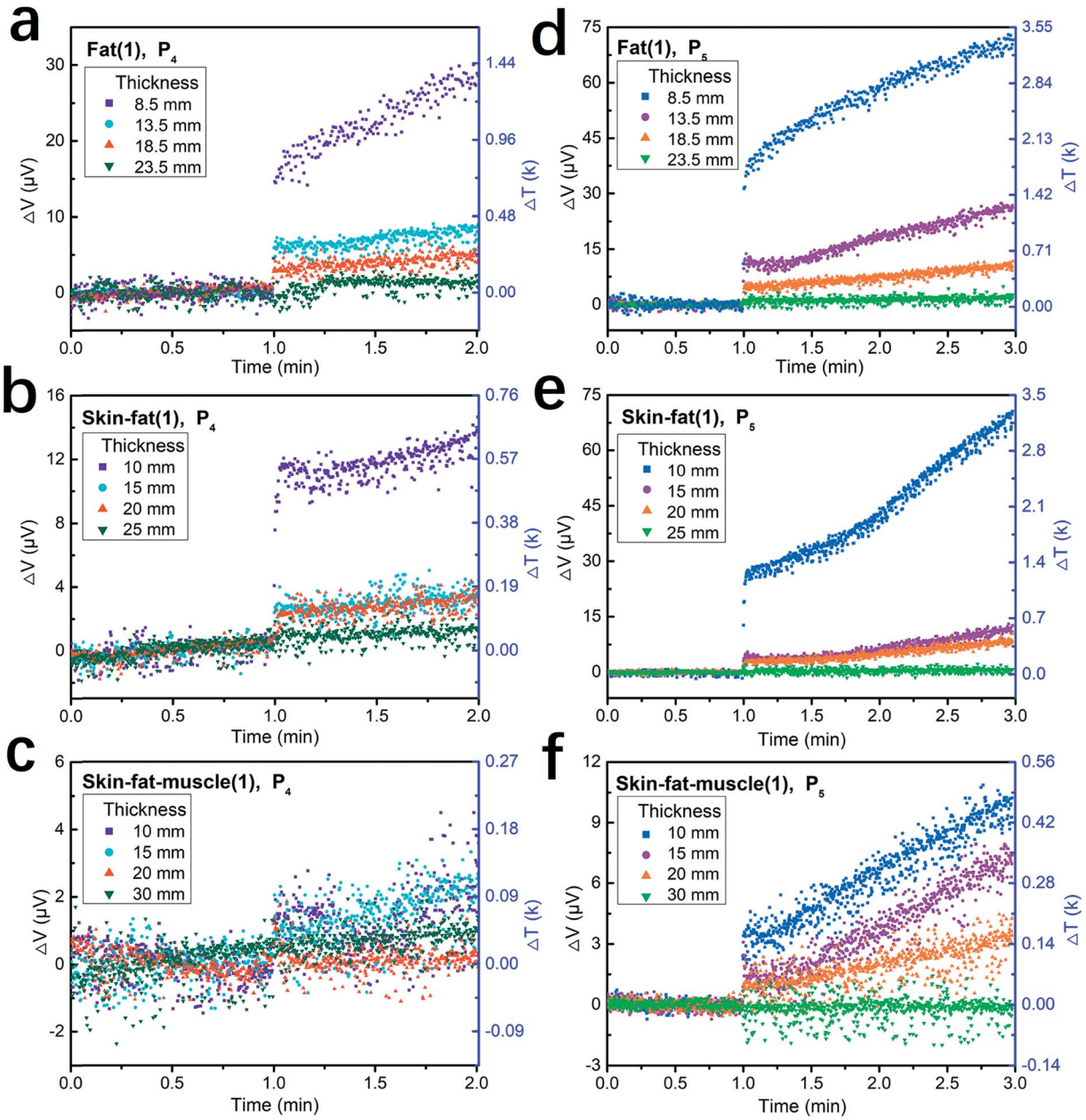

Fig. 6 Measurement results for the three types of tissue samples, namely porcine fat, skin-fat, and skin-fat-muscle with various thickness. (a)–(c) present the sensor output voltage and corresponding temperature increments for one-minute tests at a single power density of P_4, *i.e.*, 9000 W cm^{-2} (mean power density of 21.4 W cm^{-2}) and pulse frequency of 20 Hz. (d)–(f) present the results for the two-minute tests at a single power density of P_5, *i.e.*, 15 000 W cm^{-2} (mean power density of 35.6 W cm^{-2}) and pulse frequency of 20 Hz.

its intensity attenuates logarithmically with the penetration depth. As shown in Fig. 5e, the constant values of the total attenuation coefficient, μ_t, were extracted from the fitting of the normalized experimental data. According to the fittings, agarose showed an attenuation coefficient of $\mu_t = 0.101$ mm^{-1}, and the attenuation length of 10 mm for the incident 1064 nm IR laser.

After calibration of the measurement system, we measured the penetration effect and thermal effect of the 1064 nm IR laser pulses passing through thick porcine tissue. Porcine tissue was chosen because its histological appearance resembles that of human tissues. Fig. 6 shows the plots of the measurement results from three types of tissue samples, namely, porcine fat, skin-fat, and skin-fat-muscle. Fig. 6a–c present the sensor output voltage and corresponding temperature increments for one-minute tests at the single power density of P_4, *i.e.*, 9000 W cm^{-2} (mean power density of 21.4 W cm^{-2}) and pulse frequency of 20 Hz. Fig. 6d–f present the results of the two-minute tests at the single power density of P_5, *i.e.*, 15 000 W cm^{-2} (mean power density of 35.6 W cm^{-2}) and pulse frequency of 20 Hz. In this experiment, in the first minute, the laser was switched off to measure the room temperature and in the second one-minute or two-minute periods, the laser was switched on to measure the penetrating effect of porcine tissue. For the skin-fat and

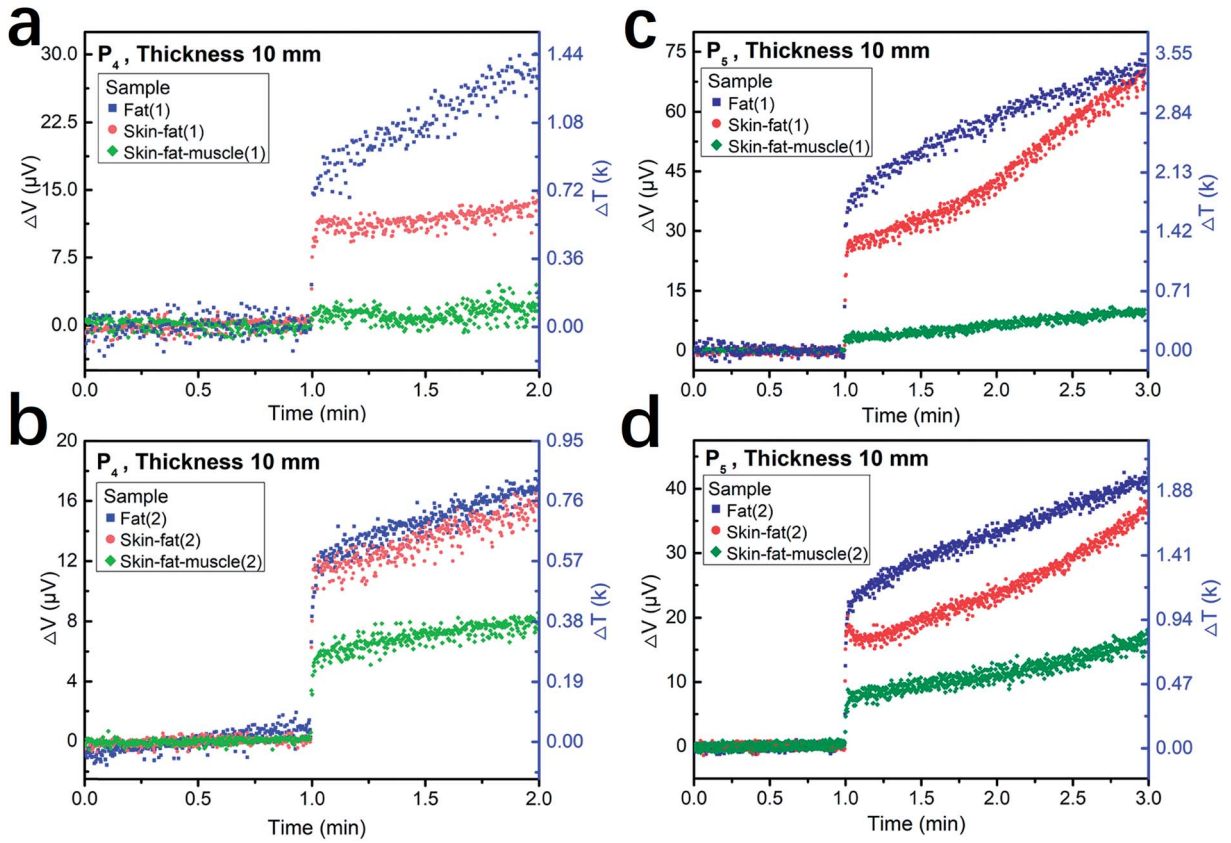

Fig. 7 Output voltage and corresponding temperature change with time at the same thickness (10 mm) for porcine fat, skin-fat, and skin-fat-muscle. (a) and (b) Experimental results for two different samples at a laser intensity of 21.4 W cm^{-2}. (c) and (d) Experimental results for two different samples at a laser intensity of 35.6 W cm^{-2}.

skin-fat-muscle samples, the thickness of the skin was kept at 1.5 mm. The results showed the near linear response of the output over the testing time.

Fig. 7 shows the plots of the measurement results for lasers penetrating 10 mm-thick porcine fat, skin-fat, and skin-fat-muscle. Fig. 7a and c show the first testing curves and Fig. 7b and d show the second testing curves. The tissues used for these two tests were taken from different shops, and the two measurements were performed within two weeks under the same laser parameters, *i.e.*, a laser intensity of P_4 (mean power density of 21.4 W cm^{-2}). Similarly, Fig. 7c and d present the results measured at a laser intensity of P_5 (mean power density of 35.6 W cm^{-2}). The blue squares, red circles and green symbols correspond to the tissues of the porcine fat, skin-fat and porcine skin-fat-muscle samples, respectively. Despite of the sample dependence and measurement errors, a common trend is clear for the same laser pulses penetrating the same thickness of tissues, where the fat allows more photons to penetrate than skin-fat and skin-fat-muscle, giving the highest laser power density, while the skin-fat-muscle shows the greatest blocking effect, resulting in the lowest laser power density.

Fig. 8 shows the plots of sensor output dependence on tissue thickness for the three types of tissues, which were tested under the laser intensity of P_5 (35.6 W cm^{-2}) and P_4 (21.4 W cm^{-2}). Fig. 8a, b and c present the data for porcine fat, skin-fat and muscle, respectively. From the data analysis, we obtained the attenuation coefficient, μ_t, for these samples, which was 0.20 ± 0.01 mm^{-1} for fat, 0.22 ± 0.03 mm^{-1} for skin-fat, and 0.29 ± 0.01 mm^{-1} for muscle. Since the tissues tested in our study were nonhomogeneous media, the temperature penetration caused by the laser was affected by the tissue mass density, tissue specific heat, thermal conductivity of the tissue and tissue blood perfusion rate.[71] However, for convenience, we still used the effective attenuation length, $L_t = \frac{1}{\mu_t}$, for a homogeneous medium to calculate the porcine tissue parameters. Accordingly, we obtained the thermal attenuation length value of 5.1 ± 0.4 mm for the porcine fat tissue, 4.7 ± 0.7 mm for the porcine skin-fat, and 3.5 ± 0.1 mm for the porcine muscle under the pulsed 1064 nm IR laser. We also measured the penetration effect through pure porcine skin tissue (thickness of about 1.5 mm) using the same laser parameters and irradiation dose, and the results are shown in Fig. S3 of the ESI.† From the following analysis, we determined the adsorption effect of porcine skin using the experimental results shown in Fig. 6–8. Fig. S3† shows that the absolute temperature increment after a 21.4 W cm^{-2} laser penetrated the porcine skin tissue for 1 min is 6.0 ± 0.4 K and that for a 35.6 W cm^{-2} laser penetrating the same tissue for 2 min is 11.6 ± 1.0 K. From the results shown in Fig. 8, it can be observed that porcine skin has smaller attenuation length for IR lasers than porcine fat.

Next, we checked the thickness-dependent local temperature increment when the 1064 nm IR laser pulses penetrated body

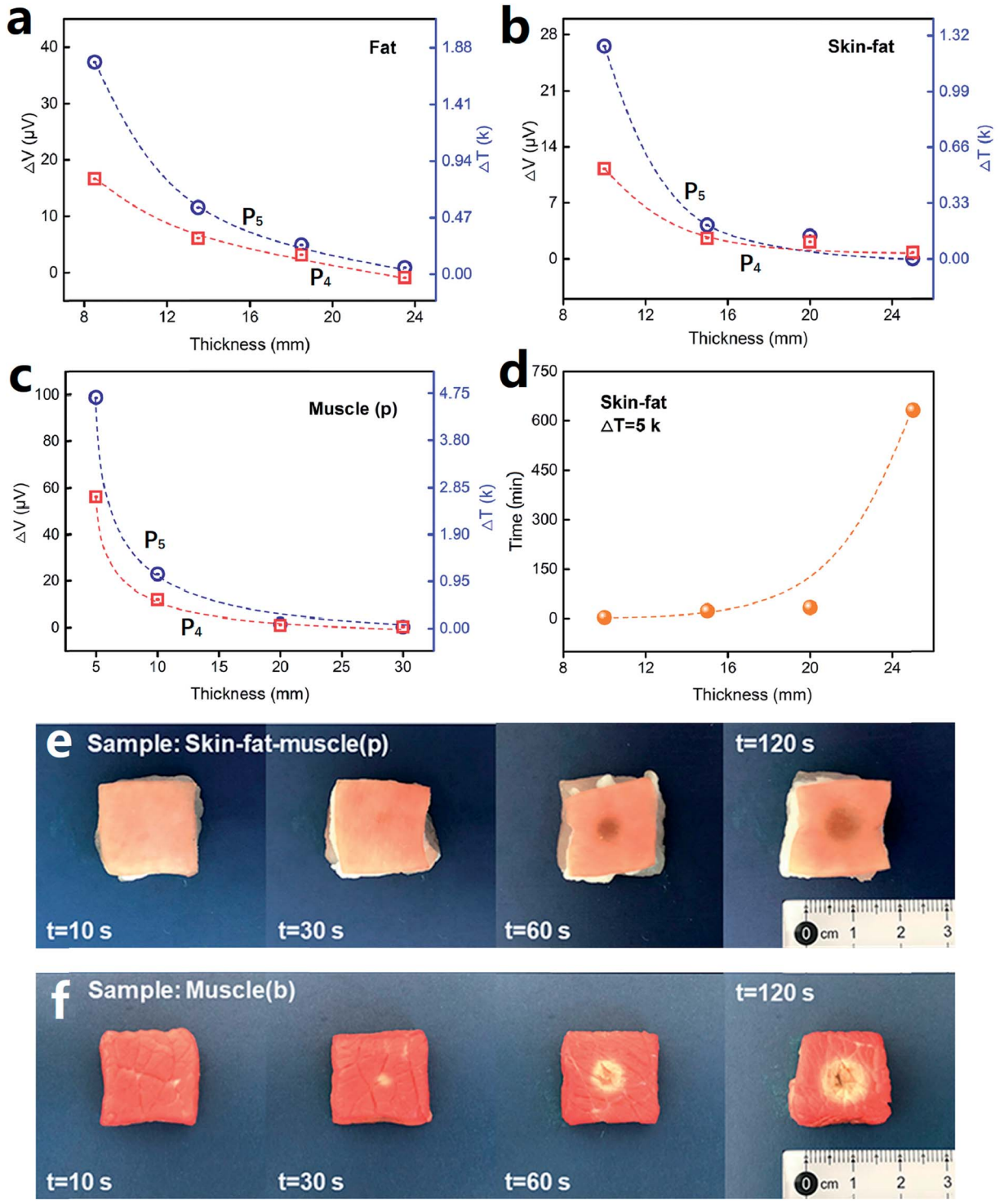

Fig. 8 (a)–(c) Sensor output dependence on tissue thickness for the three types of tissues tested under a laser intensity of P_5 (35.6 W cm^{-2}) and P_4 (21.4 W cm^{-2}). (d) Irradiation time needed for a local temperature increment of 5 K at the laser spot when it penetrates tissues of different thickness. (e) After 10 s, 30 s, 60 s and 120 s 35.6 W cm^{-2} laser irradiation, the morphology of the corresponding porcine skin tissue changes. (f) With the same time and laser intensity irradiation, the morphology of the corresponding beef muscle changes.

tissue. Taking the measurement curves at the laser intensity of 35.6 W cm^{-2} as an example (Fig. 6d–f), we can observe that with an increase in the skin-fat thickness from 10 mm to 25 mm, the increment rate of local temperature at the laser spot decreases from about 1.2 K min^{-1} to 0.01 K min^{-1}. Under the same conditions, when the laser pulses penetrate a 10 mm-thick skin-fat-muscle tissue, the increment rate of local temperature is only 0.2 K min^{-1}. However, when the thickness increases to 30 mm, the thermal effect at the laser spot is not detectable for a duration of 2 min. These results are consistent with the

extracted attenuation length of these tissues, and also clearly indicate that in high-intensity IR laser pulse percutaneous permeation treatment, photo-thermal interaction is not the major effect at deeper levels in tissue, *e.g.*, 25–30 mm under the skin.

Based on the experimental results, we calculated the irradiation time needed for a local temperature increment of 5 K at the laser spot when the laser pulse penetrates tissues of different thickness. Fig. 8d shows the plots of the results for porcine skin-fat tissue at a laser intensity of 35.6 W cm^{-2}. For instance, at the depth of 10 mm, the laser needs 3.6 min, at 15 mm, it needs 23.5 min, and when the depth of the tissue is more than 20 mm, the time needed for penetration is much longer than that for practical application.

The major types of biological tissues are optically inhomogeneous (turbid) and absorptive multilayered media with rough interfaces, which can influence light reflection and transmission in the tissue. In fact, the laser propagation within the tissue depends on the scattering and absorption properties of its components, including cells, cell organelles and different fiber and tubular/lamellar structures. The size, shape, and density of these structures, their refractive index, and the polarization state of the incident light predetermine the propagation characteristics of light in tissue. Moreover, in tissue, multiple scattering and absorption processes are responsible for laser beam broadening and eventual decay as it travels through the tissue. Due to these complex biological properties, many scientists are committed to studying the optical properties of tissues. Tuchin *et al.* used a spectrophotometer with an integrating sphere to measure the total transmittance and diffuse reflectance of human skin, subcutaneous and mucous tissues in the 400–2000 nm wavelength range. In a precise report, the laser scattering coefficient was 10–100 times larger than the absorption coefficient for tissues.[78,79]

At the skin surface, the temperature increment is expected to be much higher than that at deeper levels in tissues. We showed this with experiments on both 10 mm-thick porcine skin-fat-muscle tissue and beef muscle samples, as displayed in Fig. 8e and f. Under the same laser intensity of 35.6 W cm^{-2}, the surface of the porcine skin began to scorch after irradiation of only 30 s. When the irradiation time lasted for 120 s, the porcine skin surface significantly degraded and burn spots appeared. The experimental process is shown in Video S1 of the ESI.† The surface of the beef muscle tissue (Fig. 8f) underwent similar processes.

4. Conclusions

In summary, we developed micro-TFTC devices on freestanding Si_3N_4 windows to detect penetrating photons and study the penetration effects of high-intensity IR laser pulses through thick porcine tissue. By using calibration processes with lasers of varying wavelength in the range of 325–1064 nm, laser power of 0.002–80 mW and agarose samples with thickness in the range of 7–60 mm, we showed that our devices show a linear response in their output voltages to the incident laser intensities, making them excellent laser power density sensors for UV to IR laser beams. Moreover, the device output also indicates the local temperature under the laser spot. Using these devices, we measured the penetration effects of high-intensity 1064 nm IR laser pulses through porcine tissues, which are applied in practical clinical laser therapy for recovery from sports injury. The effective attenuation lengths at which the laser beam intensity attenuated to 1/e of the original value were measured to be 5.1 ± 0.4 mm for porcine fat, 4.7 ± 0.7 mm for porcine skin-fat combination, and 3.5 ± 0.1 mm for porcine muscle. When the tissues used in this study were thicker than 10 mm, the local temperature increment at the laser spot were negligible within the first 10 seconds. However, when the tissue was thicker than 30 mm, the laser-induced thermal effect was hard to detect. The results offer reliable references for the thresholds of irradiation doses in high-intensity IR laser pulse therapy, and also offer an alternative method for sensing both the laser power density and laser-induced thermal effect.

Conflicts of interest

The authors declare no competing financial interest.

Acknowledgements

We are grateful to Dr Gang Li for technical assistance in the use of the multiplexer circuit. We also thank Mr Di Song for his participation in the preparation of Fig. 4. This work was financially supported by the National Key R&D Program of China (Grants No. 2017YFA0701302 and No. 2016YFA0200802).

References

1 U. K. Tirlapur and K. König, *Nature*, 2002, **418**, 290.
2 M. F. Yanik, H. Cinar, H. N. Cinar, A. D. Chisholm, Y. Jin and A. Ben-Yakar, *Nature*, 2004, **432**, 822.
3 Y. Liu, K. Ai, J. Liu, M. Deng, Y. He and L. Lu, *Adv. Mater.*, 2013, **25**, 1353–1359.
4 B. B. Torma H and A. Vahlquist, *Acta Derm.-Venereol.*, 1988, **68**(4), 291–299.
5 A. R. Svobodova, A. Galandakova, J. Sianska, D. Dolezal, R. Lichnovska, J. Ulrichova and J. Vostalova, *Arch. Dermatol. Res.*, 2012, **304**, 407–412.
6 A. R. Young, *Phys. Med. Biol.*, 1997, **42**, 789–802.
7 H. B. Carol Bernstein, C. M. Payne and H. Garewal, *Mutat. Res.*, 2002, **511**, 145–178.
8 Y. Tanaka, K. Matsuo and S. Yuzuriha, *Clin., Cosmet. Invest. Dermatol.*, 2010, **3**, 143–149.
9 Y. Tanaka, K. Matsuo and S. Yuzuriha, *Clin., Cosmet. Invest. Dermatol.*, 2011, **4**, 123–130.
10 L. A. Santana-Blank, F. V. Elizabeth Rodrıguez-Santana, P. F.-A. Heberto Reyes, S. Rukos and K. E. Santana-Rodrıguez, *Clin. Cancer Res.*, 2002, **3082**(8), 3082–3091.
11 T. Ando, W. Xuan, T. Xu, T. Dai, S. K. Sharma, G. B. Kharkwal, Y. Y. Huang, Q. Wu, M. J. Whalen, S. Sato, M. Obara and M. R. Hamblin, *PLoS One*, 2011, **6**, e26212.

12 J. Joensen, K. Ovsthus, R. K. Reed, S. Hummelsund, V. V. Iversen, R. A. Lopes-Martins and J. M. Bjordal, *Photomed. Laser Surg.*, 2012, **30**, 688–694.
13 S. Martin, W. Verena, B. Daniel, B. Franziska, M. Andreas and W. Ernst, *J. Laser Micro/Nanoeng.*, 2008, **3**, 30–40.
14 L. Paris, I. Marc, B. Charlot, M. Dumas, J. Valmier and F. Bardin, *Biomed. Opt. Express*, 2017, **8**, 4568–4578.
15 R. P. Rastogi, Richa, A. Kumar, M. B. Tyagi and R. P. Sinha, *J. Nucleic Acids*, 2010, **2010**, 592980.
16 S.-L. Yu and S.-K. Lee, *Mol. Cell. Toxicol.*, 2017, **13**, 21–28.
17 Y. Xiang, B. Laurent, C. H. Hsu, S. Nachtergaele, Z. Lu, W. Sheng, C. Xu, H. Chen, J. Ouyang, S. Wang, D. Ling, P. H. Hsu, L. Zou, A. Jambhekar, C. He and Y. Shi, *Nature*, 2017, **543**, 573–576.
18 Y. A. Vladimirov, A. N. Osipov and G. I. Klebanov, *Biochemistry*, 2004, **69**, 81–90.
19 E. C. de Oliveira Guirro, M. I. de Lima Montebelo, B. de Almeida Bortot, M. A. da Costa Betito Torres and M. L. Polacow, *Photomed. Laser Surg.*, 2010, **28**, 629–634.
20 E. Mester, A. F. Mester and A. Mester, *Lasers Surg. Med.*, 1985, **5**, 31–39.
21 A. Y. Seteikin and I. V. Krasnikov, *Russ. Phys. J.*, 2006, **49**, 1139–1144.
22 M. Ith, M. Frenz and H. P. Weber, *Appl. Opt.*, 2001, **40**(13), 2216–2223.
23 L. Cummins and M. Nauenberg, *Biophys. J.*, 1983, **42**(1), 99–102.
24 C. Wang, R. Xu, W. Tian, X. Jiang, Z. Cui, M. Wang, H. Sun, K. Fang and N. Gu, *Cell Res.*, 2011, **21**, 1517–1519.
25 S. A. van Nimwegen, H. F. L'Eplattenier, A. I. Rem, J. J. van der Lugt and J. Kirpensteijn, *Phys. Med. Biol.*, 2009, **54**, 29–44.
26 P. Saccomandi, E. Schena, M. A. Caponero, F. M. Di Matteo, M. Martino, M. Pandolfi and S. Silvestri, *IEEE Trans. Biomed. Eng.*, 2012, **59**, 2958–2964.
27 Y. J. Rao, B. Hurle, D. J. Webb, D. A. Jackson, L. Zhang and I. Bennion, *In-situ temperature monitoring in NMR machines with a prototype in-fibre Bragg grating sensor system*, Optical Society of America, 1997, vol. 16, pp. 646–649.
28 F. A. Jolesz, A. R. Bleier, P. Jakab, P. W. Ruenzel, K. Huttl and G. J. Jako, *Radiology*, 1988, **168**(1), 249–253.
29 N. McDannold, *Int. J. Hyperthermia*, 2005, **21**, 533–546.
30 V. Rieke and K. Butts Pauly, *J. Magn. Reson. Imaging*, 2008, **27**, 376–390.
31 A. H. Mahnken and P. Bruners, *Int. J. Clin. Pract.*, 2011, **171**, 1–2.
32 P. Bruners, G. D. Pandeya, E. Levit, E. Roesch, T. Penzkofer, P. Isfort, B. Schmidt, M. J. W. greuter, M. Oudkerk, T. Schmitz-Rode, C. K. Kuhl and A. H. Mahnken, *Int. J. Hyperthermia*, 2012, **28**, 55–61.
33 U. Techavipoo, T. Varghese, Q. Chen, T. A. Stiles, J. A. Zagzebski and G. R. Frank, *J. Acoust. Soc. Am.*, 2004, **115**, 2859–2865.
34 R. L. Nasoni, T. Bowen, W. G. Connor and R. R. Sholes, *Ultrasonic Imaging*, 1979, **1**, 34–43.
35 S. Ueno, M. Hashimoto, H. Fukukita and T. Yano, *Ultrasound Thermometry in Hyperthermia, IEEE Ultrasonics Symposium*, 1990, vol. 3, pp. 1645–1652.
36 D. A. Christensen, *Cancer Res.*, 1979, **39**, 2325–2327.
37 F. Manns, P. J. Milne, X. Gonzalez-Cirre, D. B. Denham, J.-M. Parel and D. S. Robinson, *Lasers Surg. Med.*, 1998, **23**, 94–103.
38 D. S. Robinson, J.-M. Parel, D. B. Denham, X. González-Cirre, F. Manns, P. J. Milne, R. D. Schachner, A. J. Herron, J. Comander and G. Hauptmann, *J. Am. Coll. Surg.*, 1998, **186**(3), 284–292.
39 N. Salas, F. Manns, P. J. Milne, D. B. Denham, A. M. Minhaj, J.-M. Parel and D. S. Robinson, *Phys. Med. Biol.*, 2004, **49**, 1609–1624.
40 P. J. Milne, J. M. Parel, F. Manns, D. B. Denham, X. Gonzalez-Cirre and D. S. Robinson, *Lasers Surg. Med.*, 2000, **26**, 67–75.
41 H. Liu, W. Sun and S. Xu, *Adv. Mater.*, 2012, **24**, 3275–3279.
42 G. Li, Z. Wang, X. Mao, Y. Zhang, X. Huo, H. Liu and S. Xu, *Sensors*, 2016, **16**(7), 977.
43 R. Albertini, A. B. Villaverde, F. Aimbire, M. A. Salgado, J. M. Bjordal, L. P. Alves, E. Munin and M. S. Costa, *J. Photochem. Photobiol., B*, 2007, **89**, 50–55.
44 N. Bouzari, S. C. Davis and M. Keyvan Nouri, *Int. J. Dermatol.*, 2007, **46**, 80–88.
45 D. Gigo-Benato, S. Geuna, A. de Castro Rodrigues, P. Tos, M. Fornaro, E. Boux, B. Battiston and M. G. Giacobini-Robecchi, *Lasers Med. Sci.*, 2004, **19**, 57–65.
46 I. Garavello, V. Baranauskas and M. A. d. Cruz-Höfling, *Histol. Histopathol.*, 2004, **19**, 43–48.
47 P. Moore, T. D. Ridgway, R. G. Higbee, E. W. Howard and M. D. Lucroy, *Lasers Surg. Med.*, 2005, **36**, 8–12.
48 S. Rochkind, L. Leider-Trejo, M. Nissan, M. H. Shamir, O. Kharenko and M. Alon, *Photomed. Laser Surg.*, 2007, **25**, 137–143.
49 I. Saygun, S. Karacay, M. Serdar, A. U. Ural, M. Sencimen and B. Kurtis, *Lasers Med. Sci.*, 2008, **23**, 211–215.
50 M. Jaunich, S. Raje, K. Kim, K. Mitra and Z. Guo, *Int. J. Heat Mass Transfer*, 2008, **51**, 5511–5521.
51 pirie, China's Su Bingtian sets 6.43 Asian Record again in Dusseldorfhttps://pinoyathletics.info/2018/02/05/chinas-su-bingtian-asian-record-60m-dusseldorf/, (accessed February, 2018).
52 E. A. Lumpkin and M. J. Caterina, *Nature*, 2007, **445**, 858–865.
53 M. J. Caterina, *Am. J. Physiol.: Regul., Integr. Comp. Physiol.*, 2007, **292**, R64–R76.
54 K. Venkatachalam and C. Montell, *Annu. Rev. Biochem.*, 2007, **76**, 387–417.
55 N. R. Gavva, J. J. S. Treanor, A. Garami, L. Fang, S. Surapaneni, A. Akrami, F. Alvarez, A. Bak, M. Darling, A. Gore, G. R. Jang, J. P. Kesslak, L. Ni, M. H. Norman, G. Palluconi, M. J. Rose, M. Salfi, E. Tan, A. A. Romanovsky, C. Banfield and G. Davar, *Pain*, 2008, **136**, 202–210.
56 M. J. Caterina, T. A. Rosen, M. Tominaga, A. J. Brake and D. Julius, *Nature*, 1999, **398**, 436–441.

57 H. Xu, I. S. Ramsey, S. A. Kotecha, M. M. Moran, J. A. Chong, D. Lawson, P. Ge, J. Lilly, I. Silos-Santiago, Y. Xie, P. S. DiStefano, R. Curtis and D. E. Clapham, *Nature*, 2002, **418**, 181–186.
58 G. D. Smith, M. J. Gunthorpe, R. E. Kelsell, P. D. Hayes, P. Reilly, P. Facer, J. E. Wright, J. C. Jerman, J. P. Walhin, L. Ooi, J. Egerton, K. J. Charles, D. Smart, A. D. Randall, P. Anand and J. B. Davis, *Nature*, 2002, **418**, 186–190.
59 H. Watanabe, J. Vriens, S. H. Suh, C. D. Benham, G. Droogmans and B. Nilius, *J. Biol. Chem.*, 2002, **277**, 47044–47051.
60 A. D. Güler, H. Lee, T. Iida, I. Shimizu, M. Tominaga and M. Caterina, *J. Neurosci.*, 2002, **22**, 6408–6414.
61 F. Yang, G. Chen, S. Zhou, D. Han, J. Xu and S. Xu, *Sensors*, 2017, **17**(12), 2802.
62 I. Darian-Smith, K. O. Johnson, C. LaMotte, P. Kenins, Y. Shigenaga and V. C. Ming, *J. Neurophysiol.*, 1979, **42**, 1316–1331.
63 F. Viana, E. de la Peña and C. Belmonte, *Nat. Neurosci.*, 2002, **5**, 254–260.
64 Z. Wang, F. Yang, D. Han, G. Li, J. Xu and S. Xu, *J. Vac. Sci. Technol., B: Nanotechnol. Microelectron.: Mater., Process., Meas., Phenom.*, 2017, **35**, 041601.
65 S. Y. Xu, J. Xu and M. L. Tian, *Nanotechnology*, 2006, **17**, 1470–1475.
66 J. Xu, Z. Lei, J. Guo, J. Huang, W. Wang, U. Reibetanz and S. Xu, *Nano-Micro Lett.*, 2016, **8**, 270–281.
67 F. Yang, G. Li, J. Yang, Z. Wang, D. Han, F. Zheng and S. Xu, *Sci. Rep.*, 2017, **7**, 1721.
68 D. Han, G. Li, S. Zhou, Z. Wang, F. Yang and S. Xu, *RSC Adv.*, 2017, **7**, 9100–9105.
69 S. L. Jacques, *Phys. Med. Biol.*, 2013, **58**, R37–R61.
70 A. J. Welch, and M. J. C. v. Gemert, *Optical-Thermal Response Of Laser-Irradiated Tissue*, Springer, Germany, 2011.
71 V. V. Tuchin, *Tissue Optics: Light Scattering Methods and Instruments for Medical Diagnostics*, Bellingham, SPIE Press, 2015.
72 A. Ishimaru, *Wave Propagation and Scattering in Random Media*, IEEE Press, New York, 1997.
73 C. R. D. W. Ebert, S. K. Farrar, W. M. Johnston and a. A. L. B. A. S. Litsky, *J. Biomed. Opt.*, 1998, **3**(3), 326–333.
74 M. Chandra, K. Vishwanath, G. D. Fichter, E. Liao, S. J. Hollister and M.-A. Mycek, *Opt. Express*, 2006, **14**, 6157–6171.
75 S. C. Gebhart, W. C. Lin and A. Mahadevan-Jansen, *Phys. Med. Biol.*, 2006, **51**, 2011–2027.
76 E. A. G. A. N. Bashkatov, V. I. Kochubei and V. V. Tuchin, *Quantum Electron.*, 2006, **36**(12), 1111–1118.
77 G. M. P. a. N. Ramanujam, *Appl. Opt.*, 2006, **45**, 1062–1071.
78 A. N. Bashkatov, E. A. Genina and V. V. Tuchin, *J. Innovative Opt. Health Sci.*, 2011, **04**, 9–38.
79 A. N. Bashkatov, E. A. Genina, V. I. Kochubey and V. V. Tuchin, *J. Phys. D: Appl. Phys.*, 2005, **38**, 2543–2555.